RESEARCH ARTICLE OPEN ACCESS

Evaluating Reaction Kinetics Between Solid Booster and Dissolved Active Species in Redox-Mediated Flow Batteries Using Scanning Electrochemical Microscopy

Carla Santana Santos[1] | Nomnotho Jiyane[1] | Thomas Quast[1] | Maria Ibáñez[2] | Rubén Rubio-Presa[3] | Pekka Peljo[4,5] | Wolfgang Schuhmann[1]

[1]Analytical Chemistry—Center for Electrochemical Sciences (CES), Ruhr University Bochum, Universitätsstraße., Bochum, Germany | [2]Institute of Science and Technology Austria (ISTA), Klosterneuburg, Austria | [3]Department of Chemistry, University of Burgos, Burgos, Spain | [4]Department of Mechanical and Materials Engineering University of Turku, Turun Yliopisto, Finland | [5]Department of Chemistry and Materials Science, Aalto University, Espoo, Finland

Correspondence: Carla Santana Santos (carla.santanasantos@rub.de) | Wolfgang Schuhmann (wolfgang.schuhmann@rub.de)

Received: 15 December 2025 | **Revised:** 3 April 2026 | **Accepted:** 8 April 2026

Keywords: microelectrochemistry | rate constant | reaction kinetics | recessed microelectrode | redox targeting flow battery | redox-mediated flow batteries | scanning electrochemical microscopy | solid booster

ABSTRACT

Redox-mediated flow batteries boost energy density by utilizing dissolved redox species as charge carriers for solid charge-storage materials. This strategy strongly depends on the thermodynamics and kinetics between the solid booster and dissolved redox species. Conventional electrochemical methods often convolute intrinsic reactivity with mass transport effects, introducing complexity in determining limiting steps. We propose a strategy that confines solid boosters within recessed microelectrodes and employs scanning electrochemical microscopy (SECM) to estimate reaction kinetics between booster and dissolved active redox species. Confining the solid booster in the recessed microelectrode overcomes mass transport limitations of dissolved redox species and enables controlled polarization of the booster material, allowing deconvolution of key rate-determining factors. As an initial model system, Prussian blue-ferricyanide/ferrocyanide $[Fe(CN)_6]^{3-/4-}$ was used as solid booster and dissolved redox active species, respectively. The methodology was further explored for copper hexacyanoferrate with N,N,N-2,2,6,6-heptamethylpiperidinyl oxy-4-ammonium chloride and nickel hydroxide with $[Fe(CN)_6]^{3-/4-}$ and extended to Mn-based Prussian blue analogues in combination with organic redox species. Our results demonstrate that SECM coupled with the proposed recessed microelectrode strategy provides a powerful platform to disentangle interfacial kinetics and guide the rational design of solid booster-dissolved redox species and electrolytes for high-performance redox-mediated flow batteries.

1 | Introduction

Flow batteries are highly scalable and flexible electrochemical systems, ideal for grid-scale storage, but their energy density is intrinsically limited by the solubility of redox-active species. A promising solution is seen in integrating solid charge-storage materials, so-called solid boosters, which are charged and discharged by dissolved redox mediators, enabling significantly higher capacities [1]. Basically, the dissolved mediators undergo charging and discharging in a cell as in a typical flow battery, and they are used as shuttles to chemically oxidize or reduce the solids in the tanks. Such redox coupling of solid with dissolved species, often called redox targeting flow battery or redox-mediated flow battery, allows leveraging high specific capacity solids while maintaining decoupled energy and power scaling [1, 2].

Over the past 20 years, systems based on solid boosters to regenerate dissolved redox species were demonstrated in nonaqueous [3–11] and aqueous [12–19] redox-mediated flow batteries [20]. Wang's group [18] suggested the redox pair $[Fe(CN)_6]^{3-/4-}$ as

dissolved active species for enhancing the capacity through redox-mediated reactions with solid Prussian blue ($Fe_4[Fe(CN)_6]_3$, PB). The $[Fe(CN)_6]^{3-/4-}$/PB system demonstrates exceptional stability with a capacity retention of 99.991% per cycle and a capacity of 61.6 Ah L^{-1} [18]. In parallel, $K_{2x/3}Cu(Fe^{II}_xFe^{III}_{1-x}(CN)_6)_{2/3}$ (CuHCF) was proposed as solid booster mediated by soluble *N*, *N*,*N*-2,2,6,6-heptamethyl piperidinyl oxy-4-ammonium chloride (TEMPTMA) in an aqueous electrolyte [17]. The importance of high conductivity of the solid material increased the usage of the solid-booster capacity in a flow system [17]. The indirect redox targeting approach resulted in stable cycling, ≈95% coulombic efficiency, and high volumetric capacity (~350 C mL^{-1} or 97 Ah L^{-1}) [17]. These examples illustrate key advantages of the semi-solid flow battery strategy to enhance the energy density of batteries [21, 22]. However, the solid booster-mediated strategy also faces challenges such as meeting the required thermodynamic alignment between the potential of the dissolved redox species and the solid booster's redox plateau, which is crucial to maximize utilization of the booster's capacity [23]. Moreover, kinetics limitations at the solid–electrolyte interface and, importantly, counterion diffusion within solid phase can severely decrease the performance [2, 24].

Conventional bulk testing (cell cycling) makes it difficult to disentangle these effects or to obtain a detailed understanding of localized electrochemical behavior. Thus, there is a growing need for advanced electrochemical tools that can interrogate interfacial rate constants, considering the mass-transport limits in the particle/agglomerate at particle level. Conventional rotating disk electrodes (RDE) and porous-electrode methods are useful to a certain extent but struggle with real solid morphologies, dynamic wetting behavior, and heterogeneities of composites. These challenges have driven interest in micro- and nanoelectrochemistry approaches capable of circumventing diffusion limitation and interrogating interfacial charge–transfer processes [25–27]. Specifically, scanning electrochemical microscopy (SECM) was already successfully employed to derive understanding of the interaction of solid booster materials with the dissolved redox mediator in solid-mediated flow batteries [11, 27]. Wang's group explored SECM to determine the interfacial charge transfer rate of $LiFePO_4/FePO_4$ (solid material) undergoing lithiation and delithiation by interacting with two different redox mediators namely ferrocene/ferricenium (Fc/Fc^+) and dibromferrocene/dibromferricinium ($FcBr_2/FcBr_2^+$) [11]. The solid material was prepared in pellets at different $LiFePO_4/FePO_4$ ratios, and two different mediators were employed to provoke $FePO_4$ lithiation and $LiFePO_4$ delithiation. As expected, the derived reaction rate depended on the $LiFePO_4$:$FePO_4$ ratio [11].

We extend the application of SECM to interrogate the kinetics involved in the reaction between the solid booster and dissolved redox species. Although the spontaneity of the reaction between solid booster and dissolved redox species can be predicted based on thermodynamics, other factors such as electrical conductivity, ionic transport into and within the solid particles, as well as the driving force caused by the state of charge of the dissolved redox species may contribute to increasing the complexity of electron transfer processes and thus modulating the overall reaction kinetics. We explored the capability of the SECM to derive the kinetic rate constant and to quantify the effects of some of those parameters. SECM experiments were performed using the solid booster material confined in recessed microelectrodes (rME). Confining the solid booster within an rME overcomes mass transport limitations of the dissolved redox species toward the interface of the solid booster material [26], enables controlled polarization of the solid material, and provides the possibility to a direct interrogation of rate-limiting processes within the solid material.

2 | Results and Discussion

Interrogating electron transfer rates using SECM has advantages over conventional electrochemical techniques mainly due to mitigating mass transport limitations. A high diffusional flux of species toward the SECM tip leads to a diffusion-limited steady-state current, allowing the interrogation of the perturbation of the diffusion zone in front of the SECM tip by reactions at the investigated surface. This condition makes the tip current a reporter of sample kinetics for electron transfer using the well-known negative and positive feedback effect of SECM [28]. When approaching the SECM tip to an unbiased electronically conductive surface, the polarized SECM tip is converting, e.g. a species *R* to the oxidized form *O*. The electronically conductive surface immersed in an electrolyte with the redox species assumes a Nernst-equation-predicted potential. When the SECM tip is polarized, it converts the *R* to *O* at the thin layer close to the surface. A gradient of concentration generates a driving force for charge transfer at the (by an external devices) unbiased sample surface, if *O* and *R* are forming a reversible redox pair and the sample surface has a considerable size.

In this case, the so-called positive feedback effect, the SECM tip current increases as the distance toward the sample decreases [28]. In principle, the regeneration of the species proceeds at the diffusion-controlled rate of the dissolved species. In the case of kinetic-controlled conditions, the approach curve is unique and depends on the reaction rate at the surface, with mathematical equations describing the SECM current–distance relationship. For a first-order reaction, the normalized tip current can be fitted using expressions derived from finite-element or analytical models of SECM feedback [29, 30], where the heterogeneous kinetics constant governs the deviation from pure diffusion-controlled feedback. In practice, the approach curve transitions from the limiting case of positive feedback (fast kinetics, effectively diffusion-controlled) to negative feedback (sluggish kinetics) and by fitting the experimental curve to the theoretical model, one can quantitatively extract the kinetics constant (k, cm s^{-1}) [29, 30]. However, the regeneration of the redox pair measured at the SECM tip can be influenced by additional factors superimposing the heterogeneous electron transfer leading to a positive feedback, a catalytic regeneration reaction with the sample material may be possible, and in this case, a potential-dependence study is suggested to distinguish the interfacial processes [31]. For a primary dependence of the heterogeneous rate constant on the electron-transfer process, the feedback current increases concurrently with overpotential, allowing extraction of the heterogeneous rate constant by fitting of the approach curves [32, 33]. A lack of linearity with increasing potential indicates additional limitations in the reaction pathway, such as mass-transport restrictions or chemical steps.

In our studies of the solid booster/dissolved redox mediator systems, the SECM tip generates the discharged redox species, which reacts with the solid material within the rME, regenerating the charged species. An effective rate constant can be

extracted [11]; however, evaluation of the potential dependence may be beneficial to evaluate limiting steps in the reaction between the dissolved redox mediator and the solid booster. SECM approach curves toward the unbiased material interrogate the interfacial solid material, convoluting the positive feedback and the catalytic regeneration of dissolved redox species by the spontaneous reaction between the charged mediator and the solid material.

3 | Prussian Blue-Prussian White/$[Fe(CN)_6]^{3-/4-}$: Effect of Conductivity and Electrolyte on the Overall Kinetics

To demonstrate the capability of SECM to interrogate the solid booster confined in the rME, we explored Prussian Blue (PB)/Prussian White (PW) as solid booster and $[Fe(CN)_6]^{3-/4-}$ as the dissolved redox pair [18]. PB was confined inside the rME (Au microelectrode, 250 µm diameter), and this assembly is called PB@rME. Details of the rME fabrication are described in the experimental section. The rME was placed upside down in the specifically designed electrochemical cell, while the SECM tip was positioned near the surface of the rME from the top as schematically shown in Figure 1a. Photographs of the SECM cell and the microelectrodes are presented in Figure S1. The SECM tip (Pt microelectrode, 10 µm diameter) was characterized in 25 mM $K_3[Fe(CN)_6]$ in 0.1 M KCl (Figure S2) by recording cyclic voltammograms (CVs), which show the typical sigmoidal shape, as expected for a microelectrode achieving a limiting current governed by hemispherical diffusion. CVs of the solid@rME were registered before and after the SECM experiments, showing stable redox processes of PB/PW (Figure S3). The SECM tip works as the electrolyzer part of the flow battery, converting $[Fe(CN)_6]^{3-}$ to $[Fe(CN)_6]^{4-}$, which diffuses to the closely positioned solid@rME. The reaction between the solid PB and $[Fe(CN)_6]^{4-}$ regenerates $[Fe(CN)_6]^{3-}$, and the SECM tip response increases due to the locally higher concentration of $[Fe(CN)_6]^{3-}$. SECM approach curves were obtained by registering the SECM tip current at a constant applied potential while moving the tip toward the PB@rME (Figure S4 and Figure 1b). SECM approach curves were obtained with the unbiased and biased PB@rME. The apparent kinetic constant (k' in cm s^{-1}) was extracted using the theoretical fit of the approach curves according to literature [28–30].

Basically, the normalized tip current during the SECM approach curves is expressed as a function of the SECM tip dimension and the dimensionless tip-to-sample distance (d/a) and the dimensionless kinetic parameter $\kappa = k'a/D$, where a is the radius of

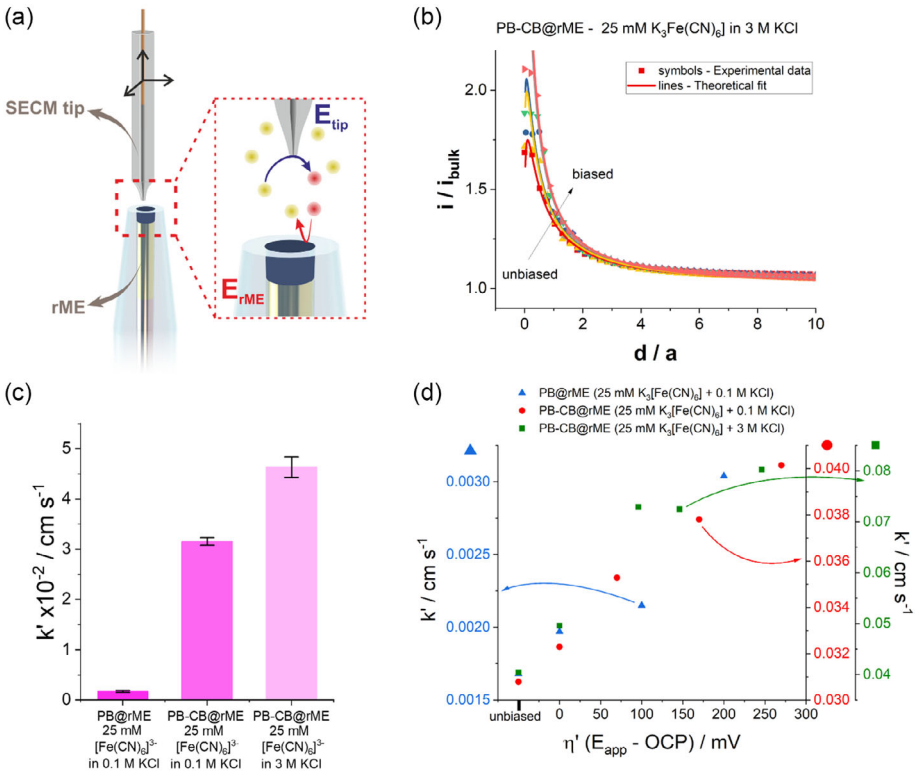

FIGURE 1 | (a) Schematic SECM setup for the evaluation of the kinetics of the reaction between the solid booster within the rMe and the dissolved redox species. The yellow dots represent the charged species, and the red dots refer to the discharged redox species: SECM tip (10 µm Pt disc microelectrode, RG 10) moved toward the top of the upside-down positioned rME filled with the solid booster material. (b) Representative SECM approach curves toward a PB-CB@rME in 25 mM mM K3[Fe(CN)6] in 3 M KCl. (b) and (c) Effective rate constant extracted by theoretical fit of the experimental SECM approach curves toward the unbiased solid@rME. The electrolyte condition is shown in the graphic, and the solid material condition is displayed on the x-axis. (d) Relation between the rate constant and η' applied to the solid@rME, derived from approach curves performed toward the rME filled with PB (blue data), PB + 10% wt. carbon black (CB) (red data, green data). SECM experiments were carried out in 25 mM K3[Fe(CN)6] in 0.1 M KCl (blue and red data) or 3 M KCl (green data). The solid@rME was unbiased or polarized at η', an overpotential relative of the OCP value, details are shown in Table S1 of the SI. Approach curves were recorded using a Pt microelectrode (diameter of 10 µm; RG 10), E*tip* = −0.2 V vs Ag|AgCl|3 M KCl.

the SECM tip and D is the diffusion coefficient of the dissolved redox mediator. By fitting the experimental approach curves to established theoretical models, the kinetic constant can be estimated. It should be noted that k′ represents an apparent kinetic constant, as it covers not only the intrinsic electron transfer kinetics between dissolved redox species and electronically conductive solid surface but also contributions arising from the regeneration of the charged dissolved redox species within the solid booster, i.e. contributions of ionic and electrical conductivities). The effect of a conductive material added to the solid active material and the availability of cations were evaluated using the SECM-solid@rME setup. Most of the solid booster materials have a low electrical conductivity and, therefore, the addition of conductive materials is commonly employed to overcome such issues [17]. However, the added conductive material can also become part of the charge transfer pathway between solid and dissolved active materials [24]. The solid material was prepared by grinding a mixture of 90% PB with 10% of carbon black (CB, C_{65} TIMCAL) and confining the mixture into the rME. Since the PB/PW redox process is a coupled ion-electron transfer reaction (CIET), the cation mobility and its insertion into the PB lattice are factors that can influence the kinetics. The electrolyte was prepared with 25 mM $K_3[Fe(CN)_6]$ in 0.1 M KCl or in 3 M KCl. The kinetic constants are provided in Table S1 and plotted in Figure 1c for the unbiased solid@rMEs. The SECM results clearly reveal the importance of the electrical conductivity of the solid booster material to enhance the reaction rates. The mean of the kinetics constant increased from 1.7×10^{-3} to 3.2×10^{-2} cm s^{-1} upon adding 10% of CB to the solid active material, and up to 4.6×10^{-2} cm s^{-1} at high ionic strength electrolyte (3 M KCl). While the addition of CB enhanced the constant by around 18 times, the use of the high cation concentration increased the kinetic constant by another 1.5 times when PB-CB@rME was employed as solid booster material. These results show the capability of the SECM to evaluate the contribution of electrical conductivity of the solid material as well the ionic strength/ion availability for the CIET reaction, which concurrently impact on the kinetics of the reaction between the solid booster and the dissolved redox mediator.

When the solid@rME was biased to an overpotential (η') with respect to the open-circuit potential (OCP) value, limiting steps of the reaction between solid and dissolved species can be evaluated. At these conditions, PB converted to Prussian White in the reaction with the $[Fe(CN)_6]^{4-}$ formed at the tip is quickly converted back to PB due to the applied potential, accelerating the regeneration of the discharged dissolved species. The rate constant increases linearly with η' for the rME filled with PB or PB-CB (Figure 1d). Note the polarization of solid material inside the rME to negative η' would provoke the reduction of PB as well as $[Fe(CN)_6]^{3-}$, which is the same reaction that occurs at the SECM tip. As expected, when the solid material inside the rME was polarized to an η' lower than OCP, a clear decrease of the magnitude of the SECM tip current during the approach curve was observed (Figure S4c) due to the redox competition between the SECM tip and PB-CB@rME [34]. Therefore, the polarization of the solid@rME to a η' to invoke the same reaction as the one at the SECM tip was avoided. A linear correlation of k' vs. η' is expected for a limiting electron transfer reaction, as also demonstrated for the bare Au microelectrode in the absence of PB or PB-CB (Figure S5). The kinetic constants extracted from the SECM approach curves toward the bare Au microelectrode were higher than those of the PB@rME, clearly showing the effect of the low electrical conductivity of the solid material as a main limitation for a high conversion rate for the reaction between the solid booster and the dissolved redox species. Standard methods cannot easily distinguish between kinetics and diffusion limited processes (Figure S6). Additionally, interpretation becomes complex due to additional effects such as ionic strength of the supporting electrolyte. It must be recognized that the CV of the PB@rME in presence of the dissolved redox species in 3 M KCl had a lower current as compared with those obtained in 0.1 M KCl, despite a better reversibility. Lower currents in high-ionic strength electrolytes were previously reported [26, 35].

The nature of the monovalent cation M^+ also plays a role for the kinetics of the CIET process of PB/PW due to insertion/extraction of the cation in the PB framework. The electrochemical kinetics of cation insertion into the PB structure were evaluated using aqueous electrolytes of KCl, NH_4Cl, and NaCl. PB-

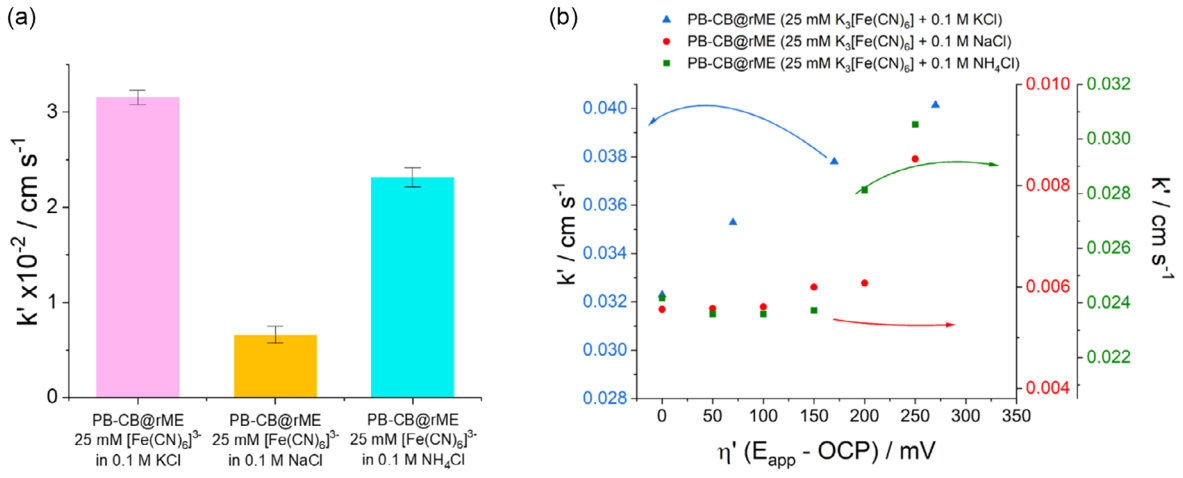

FIGURE 2 | (a) Effective rate constant k′ extracted by theoretical fit of the experimental SECM approach curves. The electrolyte condition is displayed, and the solid material is shown on the x-axis. Standard error of mean was plotted as error bars. (b) Rate constant relation between η′ applied to the PB-CB@rME in 25 mM K3[Fe(CN)6] and the electrolytes containing 0.1 M KCl (blue data), 0.1 M NaCl (red data), or 0.1 M NH4Cl (green data). SECM parameters are summarized and presented in Table S1. Potential vs. reference electrode: Ag|AgCl|3 M KCl.

CB@rME were employed to record CVs in 0.1 M electrolytes under variation of the cation (Figure S7). SECM approach curves toward the unbiased and biased PB-CB@rME are plotted in Figure S4e–f, and the influence of the cations is summarized in Figure 2, showing the clear kinetics limitation when employing NaCl compared with KCl and NH_4Cl. At unbiased rME condition (Figure 2a), the kinetic constants are 3.2×10^{-2} cm·s^{-1} for K^+, 2.3×10^{-2} cm·s^{-1} for NH_4^+, and 0.66×10^{-2} cm·s^{-1} for Na^+, which can be rationalized considering the solvation shell and the hydrated ion radii, and hydration energies of the respective monovalent cations. Potassium ions, with a hydrated radius of ~3.31 Å and a lower hydration energy (~−322 kJ mol^{-1}) [36, 37], possess a relatively weak solvation shell that is more easily disrupted, facilitating faster desolvation and insertion into the PB framework, resulting in the highest kinetics parameter (see Figure 2a).

Ammonium ions, which share a similar hydrated radius (~3.31–3.40 Å) and hydration energy (~−330 kJ mol^{-1}) [36, 37], also demonstrate good kinetics, supported by possible hydrogen bond interactions with lattice water, although the size may slightly hinder insertion compared to K^+. In contrast, Na^+ exhibits the slowest kinetics due to the stronger solvation shell, larger hydrated radius (~3.58 Å), and significantly higher hydration energy (~−406 kJ mol^{-1}) [36, 37], contributing to a greater energy barrier for desolvation and slower diffusion into the PB structure. Earlier work has suggested that Na^+ intercalates into Cu-PBA being partially hydrated, while K^+ and NH_4^+ are completely desolvated [38]. While the correlation between the k' vs. η' showed linear increase when the SECM experiments were performed in KCl, the correlation showed a more sluggish response for the electron transfer reaction in NaCl and NH_4Cl electrolyte (Figure 2b). While the results obtained with the unbiased PB@rME (Figure 2a) reveal the influence of the cation in the overall reaction between the solid material and the dissolved active species, the polarization of the PB@rME has the capability to investigate rate-limiting steps. The applied overpotential must be at least + 200 mV for NH_4^+ and + 300 mV for Na^+ to induce a change of the kinetics constant. These findings highlight that the cation mobility and ion insertion play a crucial role in the overall redox kinetics. It should be noted that residual alkali ions originating from the synthesis may remain in the framework of the solid materials and may influence both the initial state of charge and the coupled ion–electron transfer (CIET) kinetics. During SECM experiments, the use of high concentrations of alkali ions in the electrolyte and the small amount of solid material are expected to minimize this contribution. However, residual materials cannot be completely excluded, and the experimental conditions need to be considered when interpreting the apparent kinetic parameters.

3.1 | Adapting the SECM/Solid@rMEs Methodology to Alternative Solid Booster/Dissolved Redox Species

We expanded the strategy of performing SECM approach curves toward the solid@rME for other booster materials and dissolved redox species, focusing on aqueous redox-mediated flow batteries. We investigated two previously suggested systems, namely Cu hexacyanoferrate (CuHCF) as solid booster and *N*,*N*,*N*-2,2,6,6-heptamethyl piperidinyl oxy-4-ammonium chloride (TEMPTMA) as dissolved mediator [17, 27]; as well as $Ni(OH)_2$ as booster material and $[Fe(CN)_6]^{4-}$ as dissolved redox active species [19]. It is important to note that $Ni(OH)_2$ was employed as a known model system that does not undergo cation insertion like the Prussian Blue analogues; instead, the electron transfer process is dominated by surface redox reactions. Solid@rMEs were prepared with the respective active material mixed with 20% CB to increase electrical conductivity. The thermodynamic compatibility of the solid booster material and the dissolved redox species was evaluated by CVs, showing a similar redox potential in the chosen supporting electrolyte. The CuHCF-TEMPTMA system has a midpoint potential of ~+0.73 V vs Ag|AgCl|3M KCl, and $Ni(OH)_2$-$[Fe(CN)_6]^{4-}$ shows a potential of ~+0.27 vs Ag|AgCl|3M KCl (Figure S8a,b). To

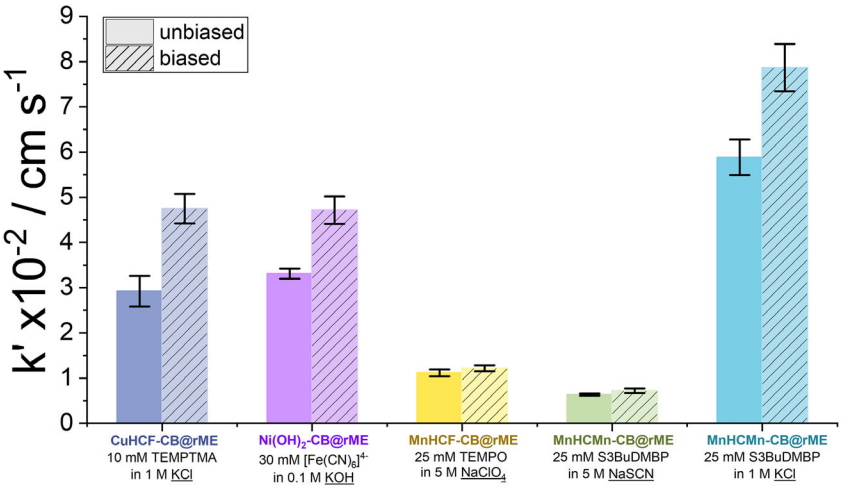

FIGURE 3 | Effective rate constant k′ extracted by theoretical fit of the experimental SECM approach curves for different solid materials confined in the recessed microelectrode (solid@rME) and dissolved redox species. Electrolyte compositions such as dissolved redox species and the supporting electrolyte chemistry are provided. The SECM approach curves (**Figure S9**) were performed while the solid@rME was unbiased (OCP) and biased at the OCP value. Potential vs. reference electrode: Ag|AgCl|3 M KCl. Standard error of mean was plotted as error bars. SECM parameters are summarized and presented in Table S2.

derive the kinetic constant, an initial control SECM approach curve toward a glass slide (insulator) was performed to obtain the diffusion coefficient of the redox mediator in the specific electrolyte (Figure S9a). Then, SECM approach curves were recorded toward the rME, and as expected, the SECM approach curves toward both CuHCF-CB@rME (Figure S9b) and $Ni(OH)_2$-CB@rME (Figure S9c) showed the predicted positive feedback. The apparent kinetic constant was higher when the solid@rME was biased at OCP values, mitigating any potentially limiting steps arising for the counter reaction. The kinetic constant for both systems was in the same order as for the PB-$[Fe(CN)_6]^{3-}$ in a K^+-containing electrolyte.

Furthermore, we proposed two potential candidate systems for redox-mediated flow batteries using on the one hand Mn-based Prussian blue analogues namely Mn^{III} hexacyanoferrate (MnHCF) and Mn^{II} hexacyanomanganate (MnHCMn) as solid boosters. Both materials were previously explored for Na-ion batteries [26, 39–41] MnHCF is a positive electrode material, while MnHCMn can be employed as negative electrode solid material in redox-mediated flow batteries. Suitable dissolved redox species were proposed based on the redox potential of MnHCF and MnHCMn, respectively, to be ~+0.45 V and ~−1.05 V vs Ag|AgCl|3M KCl (Figure S8c-e) in 5 M Na^+-containing electrolytes. For the positive material MnHCF, 2,2,6,6-tetramethylpiperidine 1-oxyl (TEMPO) was employed in 5 M $NaClO_4$. The viologen derivative 1,1′-bis(1-methyl-3-sulfonatopropyl)−3,3′-dimethyl-4,4′-bipyridinium (S3BuDMBP) was suggested as dissolved redox species for MnHCMn. For the S3BuDMBP synthesis and characterization, see details in the experimental section and in section S1 in the SI. SECM experiments were conducted as described above, with several approach curves being performed toward the unbiased solid@rME and the solid@rME biased at OCP (Figure S9 and S10). The apparent kinetic constants are provided in Table S2 and Figure 3. The kinetic constants for both systems in Na^+-containing electrolytes are lower than in K^+-containing electrolytes. Interestingly, changing the supporting electrolyte in the case of MnHCMn leads to a drastic increase in the apparent kinetic constants. Since PBA analogues undergo CIET processes, which depend on the insertion of a cation into their framework, MnHCMn showed slower kinetics in Na^+-containing electrolytes compared with K^+-containing electrolytes.

4 | Conclusions

We demonstrated an SECM methodology employing solid materials confined in rME to probe the effective kinetics of solid booster-dissolved redox mediator reactions for redox-mediated flow batteries. Confinement of the solid material overcomes mass transport limitations of dissolved species toward the solid booster interface while enabling polarization of the solid booster, thereby partially decoupling the contributions of electron transfer, ionic transport, and conductivity effects. Using PB/PW in combination with $[Fe(CN)_6]^{3-/4-}$ as a model system, we revealed the strong influence of electrical conductivity, electrolyte composition, and nature of the cation on interfacial kinetics. The approach was extended to alternative solid booster materials in combination with dissolved redox species, highlighting its versatility to assess both thermodynamic compatibility and kinetics limitations. This methodology offers a platform to deconvolute complex solid booster/dissolved active redox species interactions and provides valuable guidelines for designing efficient solid booster/dissolved active species couples for next-generation flow batteries. This methodology can be further explored for comparing active materials, designing electrolytes and evaluating experimental conditions.

5 | Experimental Section

5.1 | Chemicals, Solid Materials and Dissolved Redox Active Species

All reagents and solvents were purchased from Aldrich or Alfa-Aesar and were used as received without further purification. All solutions were prepared with milliQ water (18 MΩ cm^{-1}) and highly pure chemicals. The viologen derivative 1,1′-bis(1-methyl-3-sulfonatopropyl)−3,3′-dimethyl-4,4′-bipyridinium (S3BuDMBP) was synthesized by complete *N*-alkylation of 3,3′-dimethyl-4,4′-bipyridine with 1,3-butanesultone. General methods and full description of synthesis and characterization for the viologen derivative S3BuDMBP and its precursors are described in section **S1** in the SI (Figure S11-S18), along with the corresponding NMR spectra. Mn^{III} hexacyanoferrate (MnHCF) and Mn^{II} hexacyanomanganate (MnHCMn) were synthesized and characterized according to literature [26]. TEMPTMA was prepared and provided by the group of Prof. Hubert Girault at EPFL according to previous reports [17, 42]. Synthesis and characterization of CuHCF was reported previously [27]. More details are presented in section **S2** in the Supporting Information.

5.2 | Preparation of the Solid@rME

The recessed disc-shaped gold microelectrodes were prepared as reported before [26]. The recessed microelectrode (rME) was filled with the solid booster of interest by mechanically pressing the rME against the solid powder [26], resulting in the solid@rME. The filling procedure of solid@rME was verified by optical microscopy. CB (C_{65} TIMCAL) was added as a conductive additive to the solid booster material in a ratio of 10% wt. for PB and 20% wt. for the other booster materials: CuHCF, $Ni(OH)_2$, MnHCF, and MnHCMn.

5.3 | Electrochemical and SECM Experiments

All electrochemical measurements were performed in a four-electrode configuration using the SECM tip and the solid@rME as working electrode 1 (WE1) and 2 (WE2), respectively. A disc-shape Pt microelectrode (diameter 10 μm) was fabricated in-house and employed as WE1 (SECM tip). A Ag|AgCl|3 M KCl was employed as reference electrode (RE), while a Pt bar was used as counter electrode (CE). The SECM cell was printed with a 3D printer (filament Apollo X ASA, FormFutura) with a glass slide window to allow the visual inspection of the tip positioned on top of the solid@rME. Electrochemical measurements were performed using a bipotentiostat (IPS—bipotentiostat PGU 10 V 100 mA). The measurements were performed under exclusion of oxygen by continuous Ar purging. An inert atmosphere is essential to study the reduction process of active materials and ensures their stability. Electrochemical tests were performed at

room temperature (about 20°C). For SECM approach curves, the SECM tip was polarized at a potential to reach the diffusion limited conversion of the dissolved redox species in the specific system, while the tip was moved at an approach speed of 1 μm s^{-1} toward the solid@rME. Control SECM approach curves toward a glass slide (insulator) were performed to calculate the diffusion coefficient of the redox species in the specific electrolyte. For the kinetic constant evaluation, the solid@rME was unbiased or biased at the OCP value. Tables S1 and S2 provide the summary of the calculated apparent kinetic constants, and the details of the SECM experiments, such as the potential applied at the SECM tip, OCP values of the solid@rME in the electrolyte, and the applied potential, η', at the solid@rME. All potentials are reported vs. Ag|AgCl|3 M KCl.

Acknowledgments

The authors acknowledge funding from the European Union's Horizon Europe research and innovation programme— European Innovation Council (EIC) under the grant agreement No 101046742 (MeBattery). P.P. acknowledges the funding from the European Research Council through a Starting Grant (agreement no. 950038). Dr. Mahdi Moghaddam, University of Turku, is acknowledged for providing the CuHCF, and Prof. Hubert Girault, EPFL, is acknowledged for providing the TEMPTMA.

Open Access funding enabled and organized by Projekt DEAL.

Conflicts of Interest

The authors declare no conflicts of interest.

References

1. Z. Qi and G. M. Koenig, "Review Article: Flow Battery Systems with Solid Electroactive Materials," *Journal of Vacuum Science & Technology B, Nanotechnology and Microelectronics: Materials, Processing, Measurement, and Phenomena* 35 (2017): 40801.

2. D. Reynard, M. Moghaddam, C. Wiberg, et al., Redox-mediated Processes *Flow Batteries*. C. Roth, J. Noack, M. Skyllas-Kazacos, 2023, pp. 99–119.

3. Q. Wang, S. M. Zakeeruddin, D. Wang, I. Exnar, and M. Grätzel. "Redox Targeting of Insulating Electrode Materials: A New Approach to High-Energy-Density Batteries," *Angewandte Chemie International Edition* 45 (2006): 8197.

4. M. Duduta, B. Ho, V. C. Wood, et al., "Semi-Solid Lithium Rechargeable Flow Battery," *Advanced Energy Materials* 1 (2011): 511.

5. Q. Huang, H. Li, M. Grätzel, and Q. Wang, "DeFecT-FF: A Machine Learning Force Field Framework for High Throughput Defect Modeling in CdTe-Based Solar Cells," *Physical Chemistry Chemical Physics: Pccp* 15 (2013): 1793

6. F. Pan, J. Yang, Q. Huang, X. Wang, H. Huang, and Q. Wang, "Redox Targeting of Anatase TiO2 for Redox Flow lithium-Ion Batteries," *Advanced Energy Materials* 4 (2014): 1400567.

7. C. Jia, F. Pan, Y. G. Zhu, Q. Huang, L. Lu, and Q. Wang, "High–Energy Density Nonaqueous All Redox Flow Lithium Battery Enabled With a Polymeric Membrane," *Science Advances* 1 (2015): e1500886.

8. J. Ostrander, R. Younesi, and R. Mogensen, "High Voltage Redox-Meditated Flow Batteries With Prussian Blue Solid Booster," *Energies* 14 (2021): 7498.

9. M. Zhou, Y. Chen, Q. Zhang, et al., "Na3V2 (PO4) 3 as the Sole Solid Energy Storage Material for Redox Flow Sodium-Ion Battery," *Advanced Energy Materials* 9 (2019): 1901188.

10. Y. Zhou, G. Cong, H. Chen, N.-C. Lai, and Y.-C. Lu, "A Self-Mediating Redox Flow Battery: High-Capacity Polychalcogenide-Based Redox Flow Battery Mediated by Inherently Present Redox Shuttles," *Acs Energy Letters* 5 (2020): 1732–1740.

11. R. Yan, J. Ghilane, K. C. Phuah, et al., "Determining Li^+-Coupled Redox Targeting Reaction Kinetics of Battery Materials With Scanning Electrochemical Microscopy," *The Journal of Physical Chemistry Letters* 9 (2018): 491.

12. E. Zanzola, C. R. Dennison, A. Battistel, et al., "Redox Solid Energy Boosters for Flow Batteries: Polyaniline as a Case Study," *Electrochimica Acta* 235 (2017): 664.

13. J. Yu, L. Fan, R. Yan, M. Zhou, and Q. Wang, "Redox Targeting-Based Aqueous Redox Flow Lithium Battery," *Acs Energy Letters* 3 (2018): 2314.

14. Y. Cheng, X. Wang, S. Huang, et al., "Redox Targeting-Based Vanadium Redox-Flow Battery," *Acs Energy Letters* 4 (2019): 3028.

15. J. F. Vivo-Vilches, A. Nadeina, N. Rahbani, V. Seznec, D. Larcher, and E. Baudrin, "LiFePO4-Ferri/Ferrocyanide Redox Targeting Aqueous Posolyte: Set-up, Efficiency and Kinetics," *Journal of Power Sources* 488 (2021): 229387.

16. T. Páez, F. Zhang, M.Á. Muñoz, et al., "The Redox-Mediated Nickel–Metal Hydride Flow Battery," *Advanced Energy Materials* 12 (2022): 2102866.

17. E. Zanzola, S. Gentil, G. Gschwend, et al., "Solid Electrochemical Energy Storage for Aqueous Redox Flow Batteries: The Case of Copper Hexacyanoferrate," *Electrochimica Acta* 321 (2019): 134704.

18. Y. Chen, M. Zhou, Y. Xia, et al., "A Stable and High-Capacity Redox Targeting-Based Electrolyte for Aqueous Flow Batteries," *Joule* 3 (2019): 2255.

19. T. Páez, A. Martínez-Cuezva, J. Palma, and E. Ventosa, "Mediated Alkaline Flow Batteries: From Fundamentals to Application," *Acs Applied Energy Materials* 2 (2019): 8328.

20. S. Gentil, D. Reynard, and H. H. Girault, "Aqueous Organic and Redox-Mediated Redox Flow Batteries: A Review," *Current Opinion in Electrochemistry* 21 (2020): 7.

21. X. Wang and J. Chai, "Redox Flow Batteries Based on Insoluble Redox-Active Materials. A Review," *Nano. Mat. Science* 3 (2021): 17.

22. E. Ventosa, "Semi-Solid Flow Battery and Redox-Mediated Flow Battery: Two Strategies to Implement the Use of Solid Electroactive Materials in High-Energy Redox-Flow batteries," *Current Opinion in Chemical Engineering* 37 (2022): 100834.

23. M. Zhou, Q. Huang, T. N. Pham Truong, et al., "Nernstian-Potential-Driven Redox-Targeting Reactions of Battery Materials," *Chem* 3 (2017): 1036.

24. M. Moghaddam, S. Sepp, C. Wiberg, A. Bertei, A. Rucci, and P. Peljo, "Thermodynamics, Charge Transfer and Practical Considerations of Solid Boosters in Redox Flow Batteries," *Molecules (basel, Switzerland)*. (2021): 26.

25. C. Santana Santos, T. Quast, E. Ventosa, and W. Schuhmann, "Nanoelectrochemical Platform for Elucidating the Reaction between a Solid Active Material and a Dissolved Redox Species for Mediated Redox-Flow Batteries," *ChemElectroChem* 11 (2024): e202400283.

26. N. Jiyane, C. Santana Santos, I. Echevarria Poza, et al., "Recessed Microelectrodes as a Platform to Investigate the Intrinsic Redox Process of Prussian Blue Analogs for Energy Storage Application," *Batteries & Supercaps* 8 (2025): e202400743.

27. M. Moghaddam, L. Godeffroy, J. J. Jasielec, et al., "Scanning Electrochemical Microscopy Meets Optical Microscopy: Probing the Local Paths of Charge Transfer Operando in Booster-Microparticles for Flow Batteries," *Small (weinheim an Der Bergstrasse, Germany)* 20 (2024): e2309607.

28. A. J. Bard and M. V. Mirkin, *Scanning Electrochemical Microscopy* (Boca Raton: CRC Press, 2022), 3rd., 1–79.

29. C. Lefrou and R. Cornut, "Analytical Expressions for Quantitative Scanning Electrochemical Microscopy (SECM)," *Chemphyschem: A European Journal of Chemical Physics and Physical Chemistry* 11 (2010): 547.

30. C. Lefrou, "A Very Easy Kinetics Determination for Feedback Curves with a Microdisk SECM Tip and rather Rapid Substrate Reaction," *Journal of Electroanalytical Chemistry* 601 (2007): 94.

31. G. Wittstock, M. Burchardt, S. E. Pust, Y. Shen, and C. Zhao, "Scanning Electrochemical Microscopy for Direct Imaging of Reaction Rates," *Angewandte Chemie International Edition* 46 (2007): 1584.

32. A. J. Bard, M. V. Mirkin, P. R. Unwin, and D. O. Wipf, "Scanning Electrochemical Microscopy. 12. Theory and Experiment of the Feedback Mode With Finite Heterogeneous Electron-Transfer Kinetics and Arbitrary Substrate Size," *The Journal of Physical Chemistry* 96 (1992): 1861.

33. J. L. Fernández and A. J. Bard, "Scanning Electrochemical Microscopy 50. Kinetic Study of Electrode Reactions by the Tip Generation−Substrate Collection Mode," *Analytical Chemistry* 76 (2004): 2281.

34. K. Eckhard, X. Chen, F. Turcu, and W. Schuhmann, "Redox Competition Mode of Scanning Electrochemical Microscopy (RC-SECM) for Visualisation of Local Catalytic Activity," *Physical Chemistry Chemical Physics : Pccp* 8 (2006): 5359.

35. A. Asserghine, S. Kim, T. P. Vaid, A. Santiago-Carboney, A. J. McNeil, and J. Rodríguez-López, "Ionic Strength Impacts Charge Capacity in a Redox-Matched Flow Battery: From Single-Particle Interrogation to Battery Cycling," *ACS Energy Letters* 9 (2024): 2826.

36. Y. Marcus, "Preferential Solvation of Ions in Mixed Solvents. Part 2.—the Solvent Composition near the Ion," *Journal of the Chemical Society, Faraday Transactions 1: Physical Chemistry in Condensed Phases* 84 (1988): 1465.

37. Y. Marcus, *Ions in Solution and Their Solvation*. John Wiley & Sons, 2015, 1st., 10–62.

38. Z. Chen, Y. Zhang, F. Li, et al., "Decoding Intercalation-Chemistry Discrepancies to Couple Alkali Cations with Prussian Blue Analogue Cathodes," *Nano Energy* 141 (2025): 111097.

39. H.-W. Lee, R. Y. Wang, M. Pasta, S. Woo Lee, N. Liu, and Y. Cui, "Manganese Hexacyanomanganate Open Framework as a High-Capacity Positive Electrode Material for Sodium-Ion Batteries," *Nature Comm* 5 (2014): 5280.

40. M. Pasta, C. D. Wessells, N. Liu, et al., "Full Open-Framework Batteries for Stationary Energy Storage," *Nature Comm* 5 (2014): 3007.

41. K. Hurlbutt, S. Wheeler, I. Capone, and M. Pasta, "Prussian Blue Analogs as Battery Materials," *Joule* 2 (2018): 1950.

42. T. Janoschka, N. Martin, M. D. Hager, and U. S. Schubert, "An Aqueous Redox-Flow Battery with High Capacity and Power: The TEMPTMA/MV System," *Angewandte Chemie International Edition* 55 (2016): 14427.

43. H. Li, H. Fan, B. Hu, L. Hu, G. Chang, and J. Song, "Spatial Structure Regulation: A Rod-Shaped Viologen Enables Long Lifetime in Aqueous Redox Flow Batteries," *Angewandte Chemie International Edition* 60 (2021): 26971.

44. H. Liu, Y. Zhao, Z. Zhang, et al., "Ligand Functionalization and Its Effect on CO_2 Adsorption in Microporous Metal–Organic Frameworks," *Chemistry – An Asian Journal* 8 (2013): 778.

45. R. Rubio-Presa, L. Lubián, M. Borlaf, E. Ventosa, and R. Sanz, "Addressing Practical Use of Viologen-Derivatives in Redox Flow Batteries through Molecular Engineering," *ACS Materials Letters* 5 (2023): 798.

46. D. O. Ojwang, J. Grins, D. Wardecki, et al., "Structure Characterization and Properties of K-Containing Copper Hexacyanoferrate," *Inorganic Chemistry* 55 (2016): 5924.

Supporting Information

Additional supporting information can be found online in the Supporting Information section. The authors have cited additional references in the Supporting Information [43–46].